

NICER Spectral and Timing Analysis of 4U 1630–47 and its Heartbeat State

NINGYUE FAN,^{1,2} JAMES F. STEINER,² COSIMO BAMBI,^{1,3} ERIN KARA,⁴ YUEXIN ZHANG,² AND OLE KÖNIG²

¹*Center for Astronomy and Astrophysics, Center for Field Theory and Particle Physics, and Department of Physics, Fudan University, Shanghai 200438, China*

²*Center for Astrophysics, Harvard & Smithsonian, Cambridge, MA 02138, USA*

³*School of Natural Sciences and Humanities, New Uzbekistan University, Tashkent 100007, Uzbekistan*

⁴*MIT Kavli Institute for Astrophysics and Space Research, MIT, 70 Vassar Street, Cambridge, MA 02139, USA*

ABSTRACT

We present a spectral and timing analysis of *NICER* observations of the black hole X-ray binary 4U 1630–47 from 2018 to 2024. We find relativistic reflection features in the hard and soft intermediate states, and disk wind absorption features in the soft intermediate state and soft state. We fit the reflection features with `relxillCP` and find a stable and untruncated disk in the intermediate states; we fit the wind features with `zxipcf` and find a stable, highly ionized wind with high column density across different outbursts. Specifically, the heartbeat state is seen in two observations in 2021 and 2023 respectively. Through the phase-resolved spectral fitting, we find the flux to be correlated with the disk parameters while no strong correlation with the coronal parameters is observed, consistent with the scenario given by the inner disk radiation instability. A significant hard lag on the time scale of a second and high coherence is observed near the characteristic frequency of the heartbeat, which can be explained by the viscous propagation of mass accretion fluctuations in the disk. The positive relationship between the heartbeat fractional rms and energy can possibly be explained by a disk-originated oscillation which is then magnified by the corona scattering.

1. INTRODUCTION

Black hole X-ray binaries (BHXRBs) are binary systems in which a central stellar-mass black hole accretes mass from a companion star. During an outburst, BHXRBs are usually divided into different states: the hard state, hard intermediate state (HIMS), soft intermediate state (SIMS) and soft state based on their spectral and timing properties (Homan & Belloni 2005). The hardness - intensity diagram (HID, Belloni et al. 2011), power color diagram (Heil et al. 2015) and hardness - rms¹ diagram (HRD, Plant et al. 2014) are widely used in tracing the distinctive states of BHXRBs. Physically, different states are closely related to changes in the accretion process, as well as the outflows of the system in the form of winds and jets. The dynamic nature of the accretion process makes it possible to study the evolution of accretion geometry and the driving physics behind it (Neilsen et al. 2012).

How the disk-corona system changes structurally in different states is not clear yet. Spectral analysis is one of the useful ways to explore this question. In the hard state, the spectrum is dominated by non-thermal emission caused by the Comptonization of thermal photons off hot electrons in the corona, and the reflection of those Comptonized photons from the disk. In the soft state, thermal emission from the accretion disk is dominant. Through the modeling and fitting of different spectral components, we can analyze the properties and evolution of the system from the spectral parameters (e.g., Wang-Ji et al. 2018; De Marco et al. 2021; Liu et al. 2023; Fan et al. 2024).

Besides spectral features, studying variability on different time scales enables us to investigate the innermost region of the accretion flow (Ingram & Motta 2019). Low-frequency (LF) quasi-periodic oscillations (QPOs) with a centroid frequency in the range of 0.1-30 Hz are common in BHXRBs. The power density spectrum (PDS, derived from the Fourier transform of the light curve) is a useful way to study this behavior. Based on different features of the PDS, LFQPOs are divided into types-A, B and C (Casella et al. 2005), which appear in

Corresponding author: Cosimo Bambi
bambi@fudan.edu.cn

¹ Referring to the fractional “root mean squared” (rms) noise.

different states of the outburst (Sriram et al. 2016; Ma et al. 2021).

One characteristic QPO-like feature of particular note appears in the “heartbeat” state, for which an electrocardiogram-like light curve modulates quasi-periodically at a much lower frequency around ~ 10 mHz (Neilsen et al. 2011). The low-frequency high-amplitude oscillation is distinctive from other QPOs and is also sometimes referred to as a quasi regular modulation (QRM, Trudolyubov et al. 2001; Yang et al. 2022). The heartbeat state has only been seen in a handful of BHXRBs, including GRS 1915+015 (Neilsen et al. 2011, 2012), IGR J17091–3624 (Wang et al. 2024; Katoch et al. 2021), GRO J1655–40 (Remillard et al. 1999), and 4U 1630–47 (Trudolyubov et al. 2001; Yang et al. 2022) (on which we focus).

The underlying mechanism behind the heartbeat is not fully understood. Commonly, the heartbeat mechanism is thought to be associated with a radiation instability of the inner disk (Lightman & Eardley 1974; Done et al. 2007; Neilsen et al. 2012), a hypothesis which is broadly supported by phase-resolved and time-resolved spectral fitting (Neilsen et al. 2011; Rawat et al. 2022; Belloni et al. 1997). Moreover, the time scale of the modulation is found to be commensurate with the viscous timescale of the inner disk region (Belloni et al. 1997). Wang et al. (2024) further discussed the possibility of the heartbeat arising from the vertical disk instability in systems with a long orbital period (Życki et al. 1999) and disk tearing due to spin-orbit misalignment (Raj & Nixon 2021) in the case of IGR J17091–3624.

4U 1630–47 is a recurrent transient which typically outbursts every few hundred days (Choudhury et al. 2015; Jones et al. 1976). Previous spectral and timing studies on 4U 1630–47 have shown interesting features of this source: It has a high hydrogen column density along the line of sight, estimated to be of the order $N_{\text{H}} \approx 10^{23} \text{ cm}^{-2}$ with high resolution *Chandra* data (Gatuzz et al. 2019). Its dimensionless spin parameter has been estimated to be higher than 0.9 through both continuum fitting and reflection modeling (Kushwaha et al. 2023; King et al. 2014; Pahari et al. 2018). The inclination angle is measured to be quite high, around $\sim 64^\circ$ through reflection modeling (King et al. 2014). Prominent absorption features from disk winds are commonly seen for 4U 1630–47, e.g., in Pahari et al. (2018); Trueba et al. (2019); Kushwaha et al. (2023); Ratheesh et al. (2024). The source is mainly observed in its soft state. Through spectral and timing analysis of *INTEGRAL* and *RXTE* data, Capitanio et al. (2015) find that the hard state is missing in the 2006 and 2008 outbursts. The heartbeat state of this source was first observed in

1998 with *RXTE* (Trudolyubov et al. 2001). Yang et al. (2022) observe a clear transition from a hard-state with a low-frequency type-C QPO to the (lower-frequency) heartbeat state in 2021 with *Insight*-HXMT. Notably, for the two heartbeat states of 4U 1630–47 observed previously, the level of luminosity and hardness is similar (Yang et al. 2022).

In this paper, we focus on the spectral and timing analysis of *NICER* observations of 4U 1630–47 over the past six years. Since 2018, *NICER* has observed this source through several outbursts, and at a high monitoring cadence (see Fig. 1), which enables detailed assessment of the common patterns in its behavior.

The paper is organized as follows. Section 2 provides a detailed account of the observations and data reduction process, while Section 3 presents the applied spectral models and the corresponding results. The phase-resolved fitting of the heartbeat state is presented in Section 4 and Section 5 shows the energy-resolved timing analysis of the heartbeat state. The discussion is presented in Section 6, and the conclusion is in Section 7.

2. OBSERVATION AND DATA REDUCTION

We analyze 251 *NICER* observations of the source from 2018 to 2024. We perform the standard calibration and screening on the archival *NICER* data with `nicerl2` in `HEASOFT v6.31.1`. We use the `3C50` background model (Remillard et al. 2022). We then use the `nicerl3-spect`³ task to generate the source and background spectra, and the corresponding response files for each observation. The public software `stingray`⁴ v2.1 is used to generate the light curve in the 0.2–12 keV energy band (Fig. 1), the hardness-intensity diagram (HID, Fig. 2), and the PDS of the light curves from the original events files. The count rates of different detectors are normalized to 52-FPM equivalent intensity, and we adopt this normalization throughout this work. When computing the PDS, the time resolution of the light curves is 0.005 s, corresponding to a Nyquist frequency of 100 Hz. To create an averaged PDS from different segments of a light curve, the size of each segment is chosen to be 256 s, corresponding to a minimum frequency of about 0.003 Hz, which is enough for the study of heartbeat features at several mHz.

From the light curve, we can see that in the observations in most years, as a new outburst onsets, the count rate first rises over a period of a few weeks and

² https://heasarc.gsfc.nasa.gov/docs/nicer/analysis_threads/nicerl2/

³ https://heasarc.gsfc.nasa.gov/docs/nicer/analysis_threads/nicerl3-spect/

⁴ <https://docs.stingray.science/en/stable/index.html>

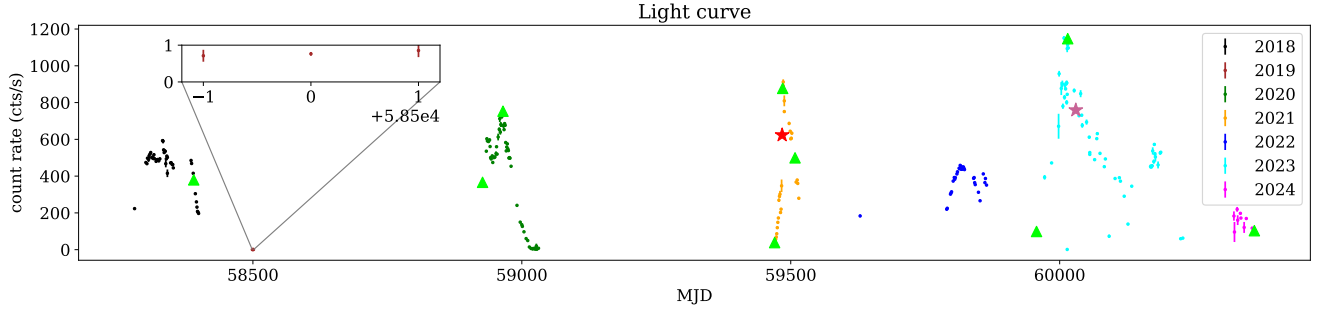


Figure 1. Light curve of the *NICER* observations of 4U 1630–47 from 2018 to 2024. Observations are colored by calendar year. The two stars mark the observations where the heartbeat is seen. Triangles mark the observations used to constrain the elemental abundances with *tbfeo* in Section 3.

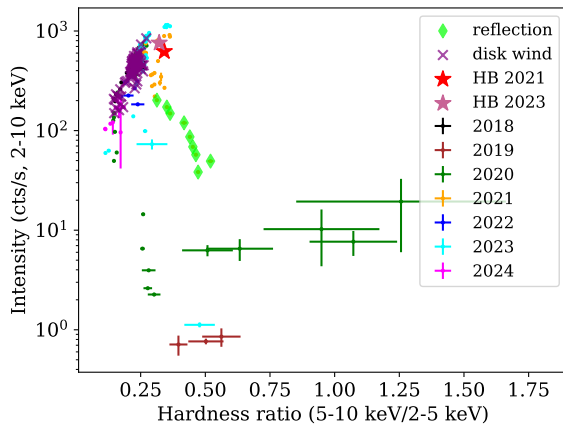


Figure 2. The HID of the *NICER* observations of 4U 1630–47 from 2018 to 2024. The hardness is defined as the ratio between the count rates in the 5–10 keV band and the 2–5 keV band. Observations are color-coded as in Fig. 1. Stars mark the observations where the heartbeat is seen. Purple crosses mark the spectra with clear disk wind absorption features, which are observed in numerous outbursts, including 2018, 2020, 2022, 2023 and 2024. Green diamonds mark observations with pronounced reflection features, which all come from in the beginning of the 2021 outburst.

later decreases over a timeframe which can be similar or much longer. Since the HID of this source does not follow the “Q”-shaped track typical of most BHXR transients, and additionally complicated by the very large column-density in the line of sight, it is challenging to distinguish different states from the HID in isolation. Therefore, we additionally explore the timing-variability features as well as the spectral features, and we show the hardness-rms (see definition in van der Klis 1995) diagram (HRD) in Fig. 3. Based on classifications of states discussed in Plant et al. (2014) for GX 339–4 with *RXTE*, Alabarta et al. (2020) for MAXI J1727–203 observed by *NICER*, Stiele & Kong (2020) for MAXI J1820 observed by *NICER* and *Swift*, and more general discus-

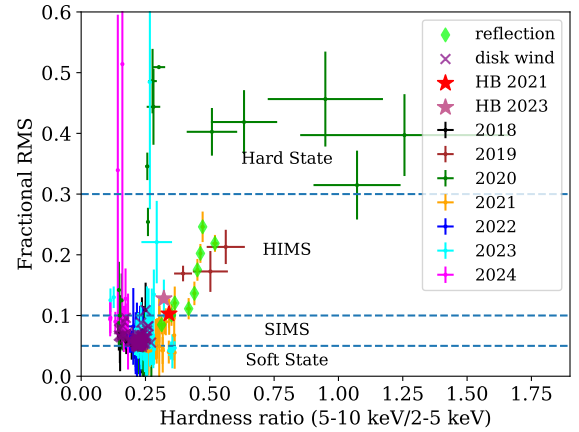


Figure 3. The HRD of the *NICER* observations of 4U 1630–47 from 2018 to 2024. The fractional rms is computed as the unbiased standard deviation of the broadband light curve divided by the mean. Color and symbol definitions are the same as in Fig. 2. The blue dashed lines show the boundary of different states, based on the classification in Plant et al. (2014).

sions in Belloni (2010); Belloni & Motta (2016), we show the distinction of different states based on the level of rms on the HRD. We find most of the observations in this 6 year-interval are in the SIMS or soft state. However, in 2021, we detect a clear transition from the HIMS to SIMS.

Among all the data obtained by *NICER*, only two observations (on September 27, 2021 (MJD 59485, ObsID 4130010115) and March 27, 2023 (MJD 60031, ObsID 6130010109) respectively) show strong heartbeat features. Their PDS (Fig. 4) show a clear, broad peak (compared to a LFQPO) at around 5 mHz, corresponding to a modulation period of around 20 s. This modulation pattern can also be clearly identified in the raw light curves of these two observation (Fig. 5). As is shown in Fig. 2 and Fig. 3, the heartbeat states of 4U 1630–47 are localized to a precise phase of the outburst, i.e., at a

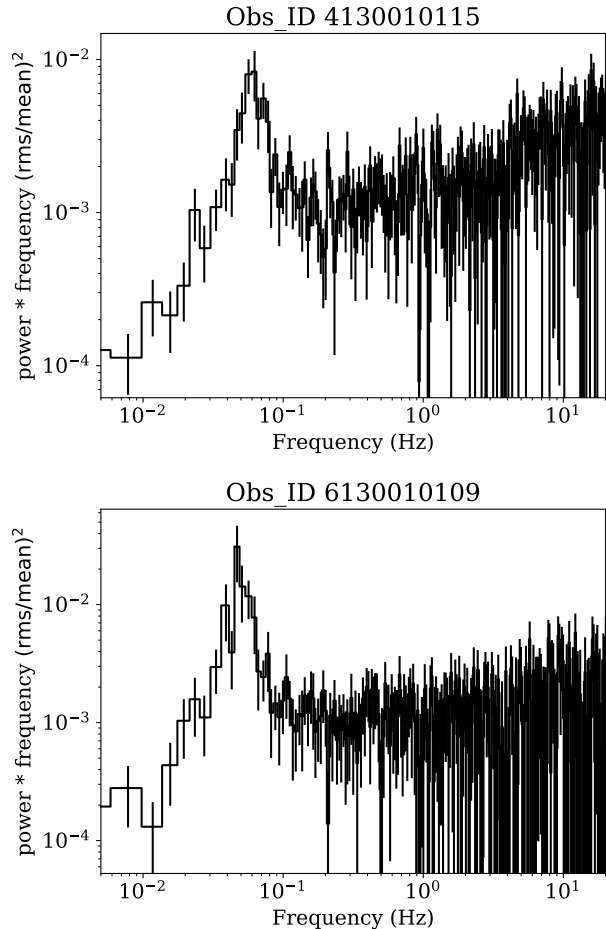


Figure 4. The PDS of the two observations when the heartbeat is observed. Observation ID 4130010115 corresponds to the observation on September 27, 2021 (MJD 59485), while Observation ID 6130010109 corresponds to the observation on March 27, 2023 (MJD 60031). We can see a clear broad peak at around 0.05 mHz in each, corresponding to a modulation period of about 20 s.

particular locus in luminosity, hardness and rms-timing variability and that locus is at the point of HIMS-to-SIMS transition.

3. SPECTRAL ANALYSIS AND RESULTS

Spectral fitting is conducted with XSPEC v12.13.0 (Arnaud 1996). We use the elemental abundances of Wilms et al. (2000) and cross-sections of Verner et al. (1996). The χ^2 statistics is used to find the best-fit values and uncertainties (throughout the paper given at a 90% confidence level) of the parameters. In the fits, we analyze the spectra in the 2–10 keV energy range. Owing to the high interstellar absorption, energies below this are dominated by the response-shelf.

3.1. Simple continuum model

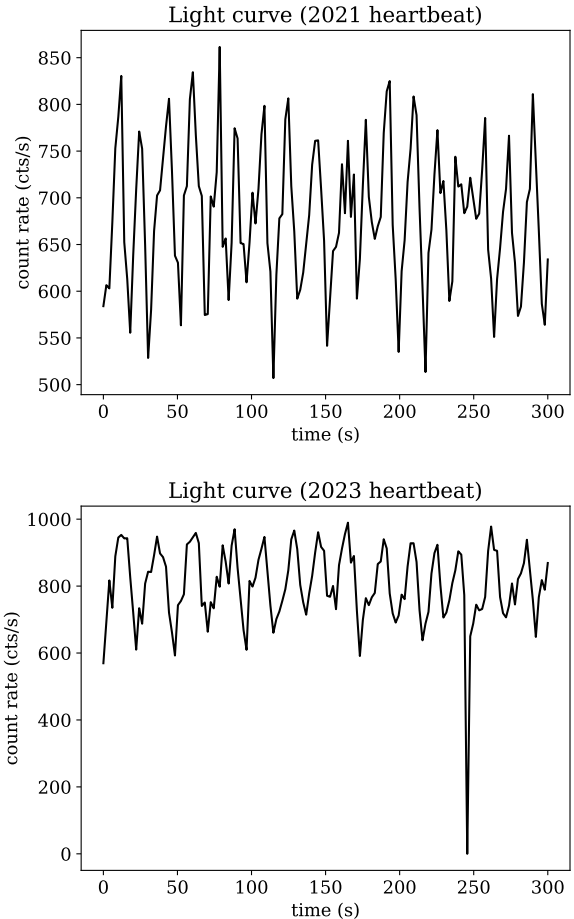


Figure 5. The 300 s light curve segments of the heartbeat states corresponding to the PDS in Fig. 4. The upper panel is the 2021 heartbeat state, and the lower panel shows the 2023 heartbeat state.

We first fit the spectra with a simple model: `tbabs` \times `diskbb`. We employ the `diskbb` model (Mitsuda et al. 1984) to fit the multi-temperature blackbody component from the accretion disk, the `tbabs` model to account for interstellar absorption (Wilms et al. 2000) with the column density N_{H} as a free parameter in the fits. We see $N_{\text{H}} \approx 10^{23} \text{ cm}^{-2}$, consistent with earlier studies (Gatuzzo et al. 2019; Pahari et al. 2018). While a significant fraction of the observations are successfully fitted with this simple model (i.e., with a reduced $\chi^2/\nu \sim 1$), most of the fits yield unacceptable fits with χ^2/ν even reaching 3–4 in some cases. This indicates that most of the spectra of this source cannot be described well by this simple model, therefore we need to adapt more complex models and take other spectral components like the Comptonization component from the corona into consideration.

We then fit the spectra with the model `tbfeo` \times `thcomp` \otimes `diskbb`, where `thcomp` (Zdziarski et al. 2020)

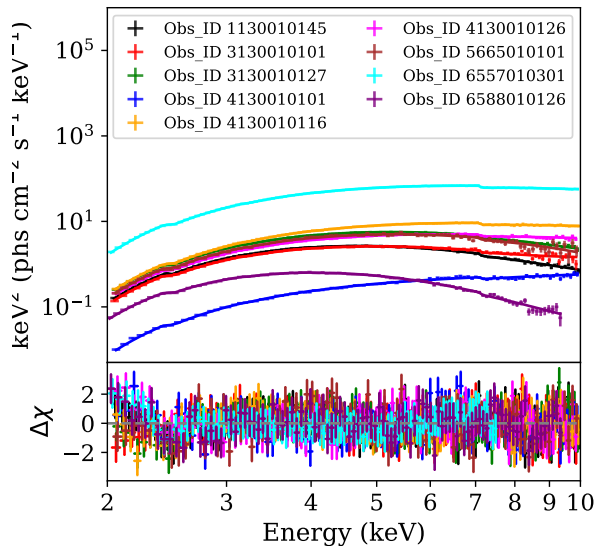


Figure 6. Fits and their residuals for the selected spectra shown with green triangles in Fig. 1 with fits using the model $\text{tbfeo} \times \text{thcomp} \otimes \text{diskbb}$. In these fits, the tbfeo parameters are linked across the spectra to obtain a robust constraint leveraging spectra with different spectral shapes.

is a convolutional model used to fit the Comptonization of thermal photons generated by the inverse Compton scattering of thermal photons off free electrons in the corona, and tbfeo is an interstellar absorption model which allows modification of the oxygen and iron abundances in addition to the hydrogen column density.

To determine the hydrogen column density and elemental abundances in tbfeo , which should be stable over time, we select nine observations spanning different accretion rates and states (three with low count rate, three intermediate, and three with high count rate. These are indicated by the green triangles in Fig. 1). We fit these simultaneously with the column density and elemental abundances in tbfeo tied together while the disk and coronal parameters are left free for each observation. The joint fit (shown in Fig. 6) gives a reduced χ^2 of $743/937 = 0.8$ (perhaps indicating that the systematic uncertainties adopted for the *NICER* processing are overestimated). From this, we obtain a column density of $N_{\text{H}} = 16.96^{+0.58}_{-0.41} \times 10^{22} \text{ cm}^{-2}$, oxygen and iron abundances of $[O] = 0.21^{+0.05}_{-0.06}$ and $[Fe] = 0.69^{+0.07}_{-0.05}$, respectively. This fit is shown in Fig 6, from which it can be seen that the model tracks our reference spectra without any obvious outlier observations performing poorly. In our subsequent analysis, we fix the parameters of tbfeo at the values obtained here. However, we note that only fitting data above 2 keV limits our ability

to robustly constrain individual elemental abundances. One can reasonably expect that O abundance fitted acts as a proxy for the aggregate of low-Z metals.

The reduced χ^2 of the fits with the model $\text{tbfeo} \times \text{thcomp} \otimes \text{diskbb}$ is shown in Fig. 7. While the reduced χ^2 of some of the fits decreases to around one, indicating that the new model is much more successful, we identify numerous outliers for which the fit remains unacceptable. The residuals of these fits reveal in several cases, clear wind absorption features (observations marked by purple crosses in Fig. 7), whereas others exhibit relativistic disk-reflection features (marked by green diamonds in Fig. 7). Further details on the quantitative definition of wind features are given in Appendix A.

The typical spectra with disk wind features and relativistic reflection features are shown in the top panels of Fig. 8 and Fig. 9, respectively. For disk wind features, there are two absorption lines between 6–7 keV (Fe XXV line at 6.69 keV and Fe XXVI line at 6.97 keV). For reflection features, a broadened iron $K\alpha$ emission line around 6.69 keV is observed. In the following two subsections, we will further discuss how we improve the fits of these spectra with disk wind absorption and relativistic disk reflection features.

3.2. Disk wind absorption features

We use the multiplicative absorption model zxcipcf (Reeves et al. 2008) to model absorption by an ionized wind. There are around 70 spectra in total showing wind absorption features, and they are mostly in the SIMS and soft state (see Fig. 3). The model we adopted to fit these spectra is: $\text{tbfeo} \times \text{zxcipcf} \times \text{thcomp} \otimes \text{diskbb}$, and the fitting results are shown in Fig. 10. The covering fraction of the wind over the source is high and touches the upper bound of 1 in most cases (annotated with red arrows). The column density of the wind is $\log N_{\text{H,wind}} \approx 24 \pm 1 \text{ cm}^{-2}$, and the ionization parameter $\log \xi \approx 5 \pm 1$. From year-to-year, no significant evolution is apparent in the properties of the wind. Our results are consistent with those obtained using a different model by Ratheesh et al. (2024), in which they use the absorption model cloudy (Ferland et al. 2017) and also find that $N_{\text{H}} \approx 10^{24} \text{ cm}^{-2}$ and $\xi \approx 10^5$.

3.3. Relativistic reflection features

We use the relativistic reflection model relxillCp (García et al. 2014) to fit the the reflection features. From 2018 to 2024, there are only 9 *NICER* observations showing a clear reflection component, which are observed during the HIMS to SIMS state transition at the beginning of the 2021 outburst. The model used to fit these spectra is $\text{tbfeo} \times \text{thcomp} \otimes (\text{diskbb} +$

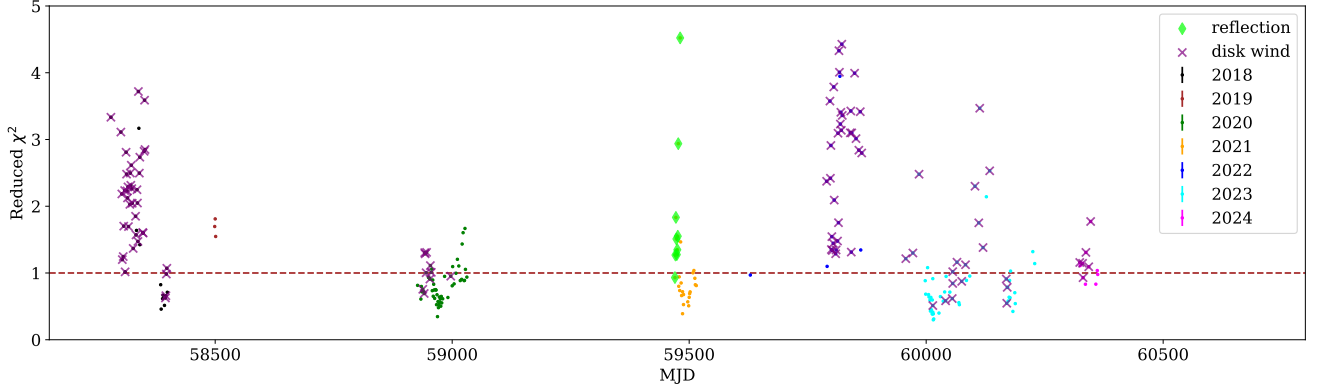


Figure 7. The reduced χ^2 of the fits with the model $\text{tbfeo} \times \text{thcomp} \otimes \text{diskbb}$. The purple crosses mark the spectra with clear disk wind absorption features. The green diamonds mark the spectra with reflection features.

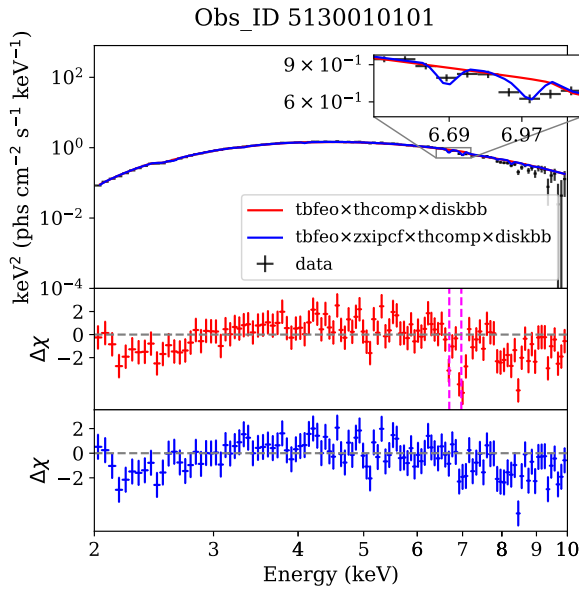


Figure 8. A typical and representative spectrum with disk wind features, taken from Observation ID 5130010101 obtained on July 30, 2022 (MJD 59786). The top panel shows the fits with (blue) and without (red) having included a wind component. The two magenta dashed vertical lines mark the 6.69 keV Fe XXV line and 6.97 keV Fe XXVI line. The bottom two panels show the residuals from both fits.

relxillCp). To avoid the degeneracy between the inner disk radius and the spin (Buisson et al. 2019), we fix the spin at the maximum value 0.998 in relxillCp and study the change of R_{in} . The inclination angle is fixed at 64° (King et al. 2014). The reflection fraction is set to -1 so that only the reflection component is produced (noting that the Comptonized emission is already described by $\text{thcomp} \otimes \text{diskbb}$). The coronal temperature kT_e and photon index Γ in the Comptonization component and reflection component are linked to-

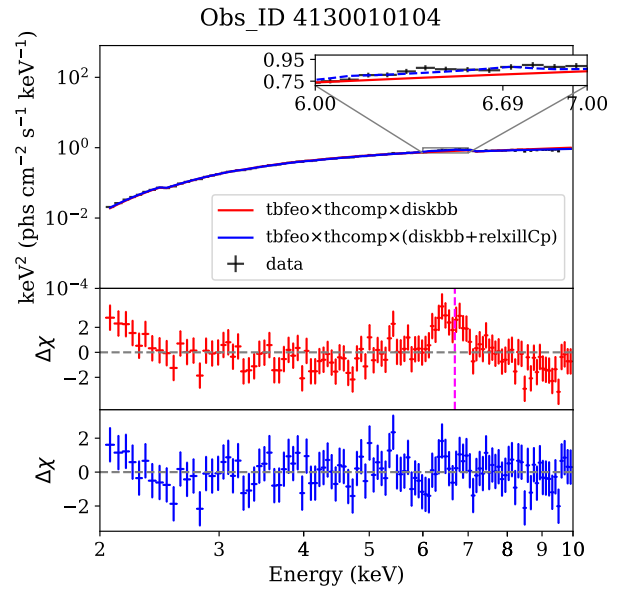


Figure 9. A typical and representative spectrum with relativistic reflection features, taken from Observation ID 4130010104 obtained on September 16, 2021 (MJD 59475). The top panel shows the fits with (blue) and without (red) having included a reflection component. The magenta dashed vertical line marks Fe XXV at 6.69 keV. The bottom panel shows the fitting after the reflection component relxillCp is added.

gether. Due to the lack of data higher than 10 keV, the corona temperature cannot be constrained well from the fits, so we fix it at a reasonable benchmark of 50 keV. The emissivity of the reflection component is modeled with a power law ($\epsilon \propto r^{-q}$).

The fitting results for these nine spectra are shown in Fig. 11, from which we can see how the disk and corona evolve during the state transition from the HIMS to SIMS. The photon index Γ changes from around 1.7

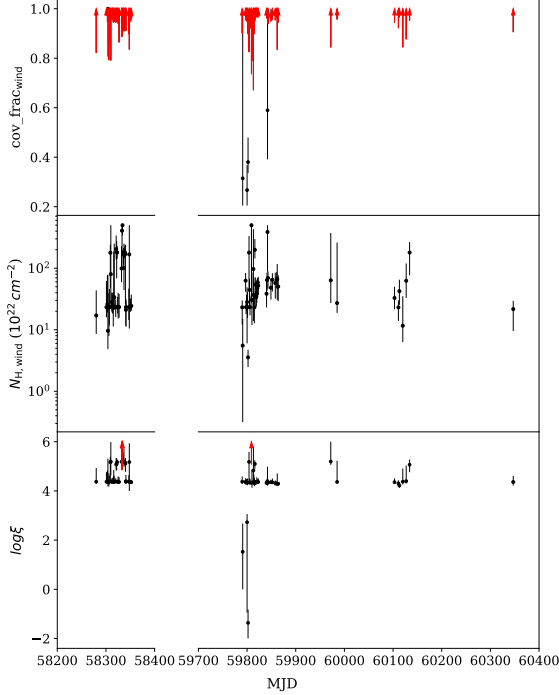


Figure 10. Fitting results of the parameters in the model $\text{tbfeo} \times \text{zxcipcf} \times \text{thcomp} \otimes \text{diskbb}$. The parameters are (from top to bottom): the covering fraction, the column density, and the ionization degree of the wind. Points touching the upper bound of the fit are annotated with red arrows.

(which is the typical value of Γ in the harder states) to higher than 2 (which is the typical value of Γ in the softer states). For the thermal component, while the inner disk temperature does not change much, the normalization factor of diskbb increases. Concerning the ongoing debate on whether the disk is truncated or not in the hard state and intermediate states (Fabian et al. 2014), our results here indicate that the inner disk radius R_{in} given by the reflection component is stable and near the innermost stable circular orbital (ISCO) in the HIMS to SIMS transition.

Meanwhile, in the first 7 observations in the HIMS, an increasing trend of the reflection emission index q is observed while the covering fraction of the corona is decreasing, indicating a possible scenario that the reduced spatial extent of the corona makes the reflection emission more concentrated centrally.

3.4. Fitting results of the thermal component

We summarize the results of fitting the thermal component with diskbb for all the observations in Fig. 12. Generally, the inner disk temperature is anti-correlated with the diskbb normalization factor. At the end of the 2020 observations and the 2019 observations, the inner disk temperature decreases to a quite low value at

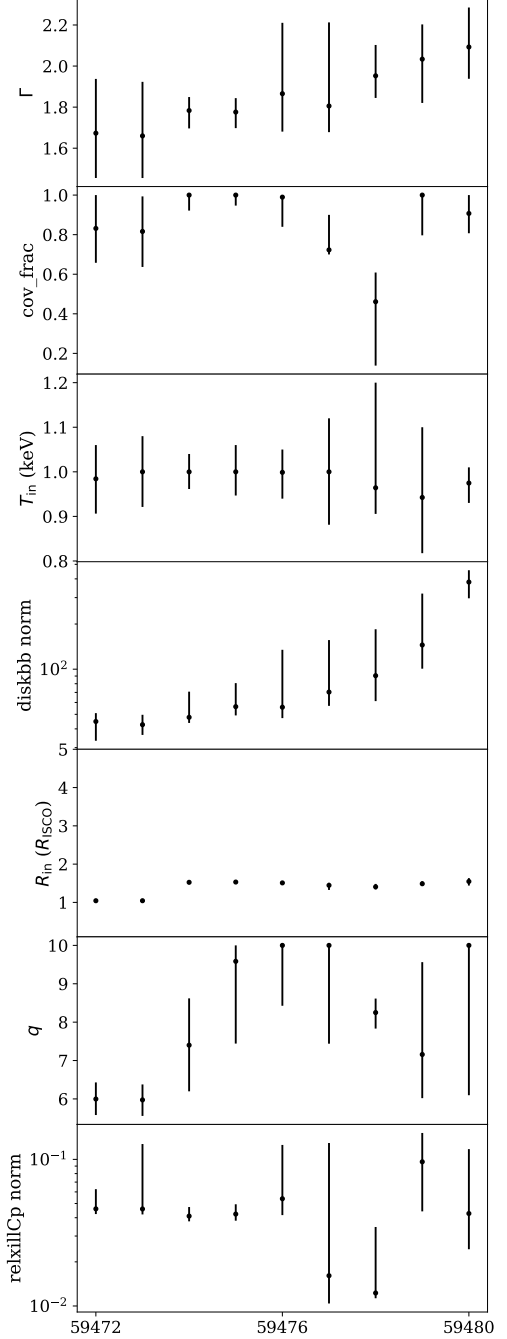


Figure 11. Fitting results of the parameters in the model $\text{tbfeo} \times \text{thcomp} \otimes (\text{diskbb} + \text{relxillCp})$. The parameters are (from top to bottom): the photon index Γ , the covering fraction of the corona over the disk, the inner disk temperature, the normalization factor of the disk component, the inner disk radius in units of R_{ISCO} for a Kerr black hole with $a_* = 0.998$ given by relxillCp , the reflection emissivity index q , and the normalization of the reflection component.

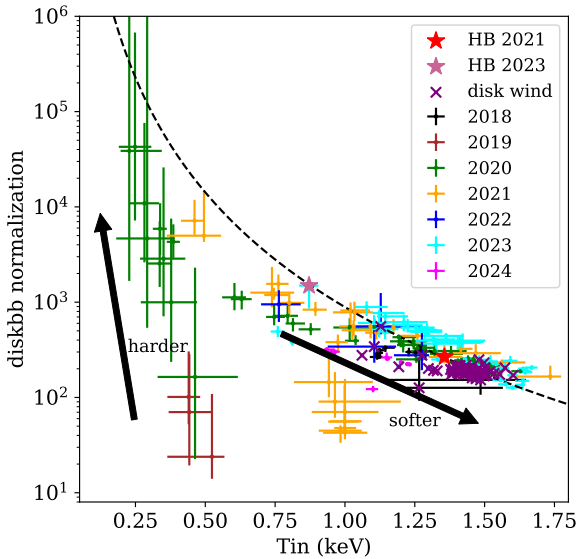


Figure 12. The fitting results showing the relationship between the inner-disk temperature and the disk normalization. The dashed line show constant R_{in} contours, calculated from the equation $norm_{\text{diskbb}} = (R_{\text{in}}/f_{\text{col}}^2 D_{10})^2 \cos i$ (Kubota et al. 1998) and adopting a temperature-dependent color correction factor $f_{\text{col}} \propto T_{\text{in}}^{1/4}$ (Davis et al. 2006).

around 0.2 keV and the normalization factor of `diskbb` increases when the source returns from the soft state to the hard state (see lower right points in the HID in Fig. 2). The estimates for these lower-temperature points ($T_{\text{in}} \lesssim 0.4$ keV) have large systematic uncertainties due to the exclusion of low-energy data and the low total counts in these spectra. When the source becomes brighter in the soft state, the inner disk temperature and the `diskbb` normalization factor change in an inverse manner. For most of the time, the inner disk temperature is higher than 1 keV, indicating the dominance of the soft state of the source, which is also found in Capitanio et al. (2015) through spectral-timing analysis of the 2006, 2008 and 2010 outbursts of 4U 1630–47.

It is worth noting that despite the similarity in the hardness, luminosity and timing properties between the two heartbeat states, we find they have quite different spectra and thermal features. We note that for both the 2021 and 2023 outburst, sudden and large-amplitude changes in the inner disk temperature before, during and after the heartbeat state are observed (further details about the spectral and temperature change can be found in Appendix B). In Section. 6, we explore possible explanations for this large temperature shift.

4. PHASE-RESOLVED FITTING OF THE HEARTBEAT STATE

In order to explore the physical changes during the quasi-periodic heartbeat oscillation, we follow the approach in Neilsen et al. (2011, 2012) to achieve a phase-folding to then determine phase bins with corresponding spectra we can analyze. In this approach, we first pick out one typical cycle and calculate its cross correlation against the entire light curve. The maxima of the cross correlation function indicate starting points of new cycles. Based on Neilsen et al. (2011), we choose the time with the highest count rate as the start of each period, corresponding to phase $\phi = 0$. We then fold the entire light curve according to the starting points we have found, and iterate to achieve a new template profile each time by averaging the heartbeat cycles. This process of finding the starting points and calculating the averaged light curve in one period is iterated several times until we find an almost stable folded light curve.

For each heartbeat observation, we employ a light curve of 300 s (Fig. 5) to calculate the folded light curve. The oscillation period of the heartbeat in 2021 is about 18 s, and the period of the heartbeat in 2023 is about 20 s, which allows for more than 10 values for each phase and yields adequate statistics for phase-resolved fitting. The folded light curves are shown in Fig. 13. Each phase bin corresponds to 2 s in an average period, so the folded light curve for the observation in 2021 has 9 bins, while the one for 2023 has 10 bins. Based on the folded light curves, we extract the data in different phases from different oscillation periods using the `extractor`⁵ command in `heasoft` and combine all the data from the same phase together to derive the phase-resolved spectra. Each spectrum has more than 20000 counts on average. We then perform fits on each phase bin to obtain the spectral parameter evolution for different phases. In the following, we will present the phase-resolved fitting results with different models.

4.1. Non-relativistic thermal model

In this part, we fit the phase-resolved spectra with the model: `tbfeo` \times `thcomp` \otimes `diskbb`. We calculate the correlation coefficient between the count rate and spectral parameter using the Pearson correlation coefficient. The error of the correlation coefficient is calculated at 1σ level. For both the heartbeat in 2021 and 2023, the count rate shows positive correlation with the inner disk temperature and negative correlation with the `diskbb` normalization factor, indicating that during the heart-

⁵ <https://heasarc.gsfc.nasa.gov/lheasoft/ftools/headas/extractor.html>

beat oscillations, the higher the flux is, the smaller the inner disk radius is and the higher the inner disk temperature is. However, the coronal parameters are not observed to be correlated with the count rate at 1σ level in both heartbeats. How disk spectral parameters change with phase given by the fits is shown in Fig. 14.

4.2. Relativistic thermal component

In order to see whether the fitting results are affected by the choice of the thermal component, we next replace `diskbb` with `kerrd`. `kerrd` describes the optically thick accretion disk around a Kerr black hole (Ebisawa et al. 2003). Compared with the commonly used relativistic disk model for a Kerr black hole `kerrbb` (Li et al. 2005), the inner disk radius is also a free parameter in `kerrd`, thus enabling us to see the evolution of inner disk radius directly instead of estimating it from a non-relativistic thermal model or changes in spin. Meanwhile, the mass accretion rate parameter in `kerrd` allows us to see dynamical changes in the accretion process.

With the model `tbfeo` \times `thcomp` \otimes `kerrd`, the changes of the coronal parameters are consistent with the previous ones despite the difference in the choice of the thermal model. At $\gtrsim 90\%$ confidence, we can see that the count rate is negatively correlated with the inner disk radius and positively correlated with the mass accretion rate, as shown in Fig. 15.

5. TIMING ANALYSIS OF THE HEARTBEAT STATE

5.1. Energy-resolved PDS

We further explore the timing properties of the heartbeat state, first computing the PDS for photons in different energy bands. We fit each with a Lorentzian model, which is commonly used to fit PDS including those with QPOs (Bachetti & Huppenkothen 2022). For the PDS in the heartbeat state, the variability can be modeled with three Lorentzian functions. We set a zero-centered Lorentzian for the broad band noise, one peaked at the heartbeat characteristic frequency, and a third to fit the noise at higher frequencies.

The energy-resolved PDS and the corresponding energy-dependent fractional rms (here computed from the square root of the Lorentzian normalization) of the heartbeats are shown in Fig. 16. The fractional rms corresponds to the amplitude of the heartbeat oscillation, and is found to be positively correlated with energy, while there is no clear correlation observed for the other two Lorentzian parameters.

5.2. Energy-resolved time lag and coherence

Analysis of the lags between the photons of different energies is a powerful tool to study the origin of

variability in data (Wang et al. 2021; Bollemeijer et al. 2024; Ma et al. 2021), including heartbeats (Yang et al. 2022). In addition, coherence measures the degree of linear correlation between two time series (Bachetti & Huppenkothen 2022), enabling us to assess the strength of the correlation between the oscillations of light curves of different energy bands. Here we choose the reference energy band to be 2–3 keV. We use `stingray` to calculate the frequency dependence of the lag and coherence of the chosen energy bands (3–4 keV, 4–7 keV, 7–12 keV) versus the reference energy band in the heartbeat states in 2021 and 2023, and the results are shown in Fig. 17. From the coherence, we can see that the light curves of different energy bands are relatively highly linearly correlated (coherence $\gtrsim 0.8$) near the characteristic frequency of the heartbeats annotated by the yellow region. A significant hard lag of ~ 1 s between 4–12 keV photons and 2–3 keV photons is clearly observed near the heartbeat frequency.

6. DISCUSSION

6.1. The change of the inner disk radius in different states

If we naively derive the inner disk radius from the `diskbb` normalization factor using the formula $norm_{\text{diskbb}} = (R_{\text{in}}/D_{10})^2 \cos i$, it should be concluded from Fig. 12 that R_{in} becomes smaller when the system becomes softer in the soft state.

While at lower temperatures the disk emission can generally be well described by a multi-temperature disk blackbody spectrum, non-thermal effects such as the Compton scattering in the disk atmosphere may produce deviations from the multi-temperature disk blackbody spectrum, especially when the inner disk temperature is high. This is normally taken into account by introducing a color correction factor f_{col} (also called spectral hardening factor) (Shimura & Takahara 1995; Kubota et al. 1998). Moreover, it has been found in previous studies that the color correction factor has strong dependence on the disk temperature (Kubota & Makishima 2004; Davis et al. 2006), which can be approximately described by $f_{\text{col}} \propto T_{\text{in}}^{1/4}$. Based on this scaling relation and the equation $norm_{\text{diskbb}} = (R_{\text{in}}/f_{\text{col}}^2 D_{10})^2 \cos i$ (Kubota et al. 1998), we overlay the constant R_{in} contour in Fig. 12, showing that R_{in} is essentially constant when the system is in the soft state. Similar results have also been found in Swift J1727–1613 (König et al. 2025, in preparation). We note a long-history of evidence from the thermal disk emission for soft states exhibiting a stable accretion-disk inner radius (e.g., detailed analysis of several decades of observations of LMC X–3; see Steiner et al. (2010), and references therein).

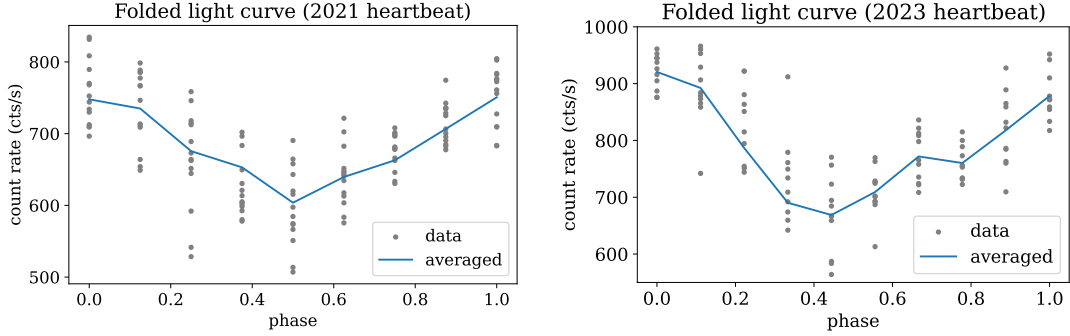


Figure 13. The phase-folded light curves for the 2021 heartbeat state (left) and 2023 heartbeat state (right). Gray points show the phase-mapped individual oscillations. The blue line shows the averaged folded light curve.

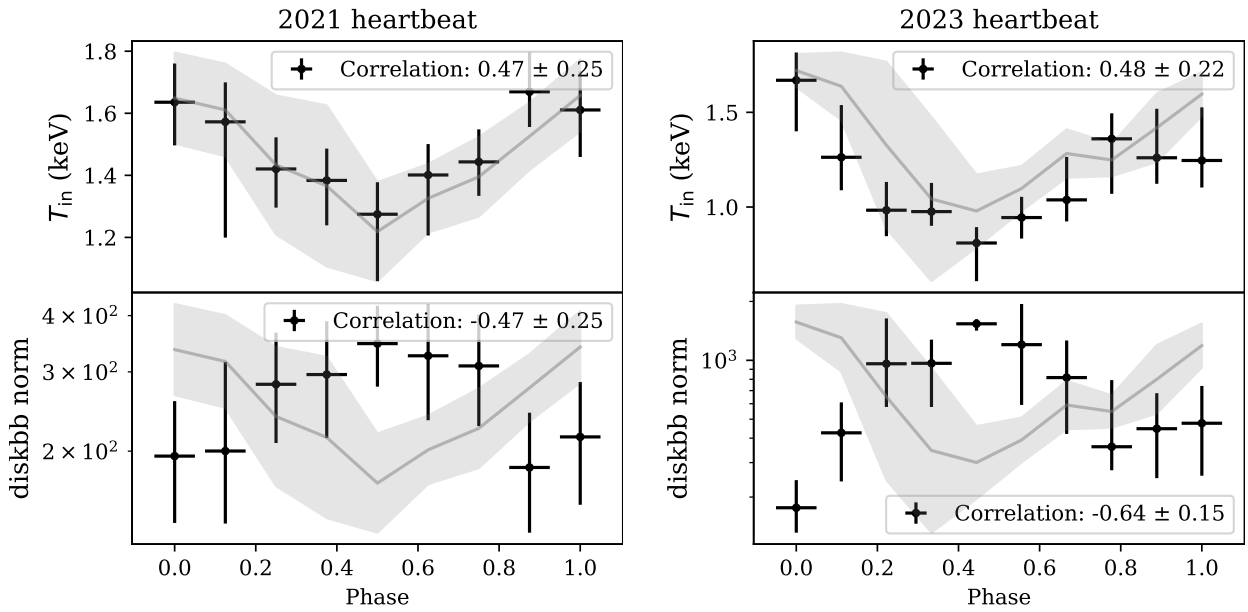


Figure 14. The changes of disk parameters with phase in one heartbeat oscillation, fitted using the model $\text{tbfeo} \times \text{thcomp} \otimes \text{diskbb}$ for the 2021 heartbeat state (left) and 2023 heartbeat state (right). The phase-folded lightcurve is overlaid in gray as a reference. The inner disk temperature (T_{in}) is shown in the upper panels, and the disk normalization factor is shown in the lower panels. Pearson-correlation coefficients are shown for each, depicting the correlation between the phase-folded light curve profile and the spectral parameters.

6.2. Heartbeat mechanism

Inner disk radiation instability is a popular candidate mechanism for producing the heartbeat oscillation (Lightman & Eardley 1974; Done et al. 2007; Neilsen et al. 2012). In that scenario, the dominance of the radiation pressure in the inner disk region and the lack of balancing mechanism gives rise to a thermal-viscous instability cycle resulting in the heartbeat oscillations in the light curve (Done et al. 2007; Neilsen et al. 2011).

To gain a better understanding of different physics processes behind this cycle behavior, it is useful to refer to the “S-curve” showing the relationship between the mass and temperature at a certain disk radius (e.g., see Fig. 7 in Done et al. 2007). The curve has three

branches: a lower viscous slow rise (where the heating is balanced by radiative cooling and the temperature increases slowly with mass), an upper slow viscous fall (where the heating is balanced by advective cooling and the temperature decreases slowly with mass) and the middle thermal viscous cycle (where the accretion process switches quickly between the two stable branches) (Wang et al. 2024). This cycled oscillation causes a density wave to propagate along the disk and results in the fast changes in the mass accretion rate, inner disk radius, and temperature. The fast variability of disk parameters in our phase-resolved fitting results (Sect. 4) is consistent with the scenario given by the radiation pressure instability theory. Previous phase-resolved and

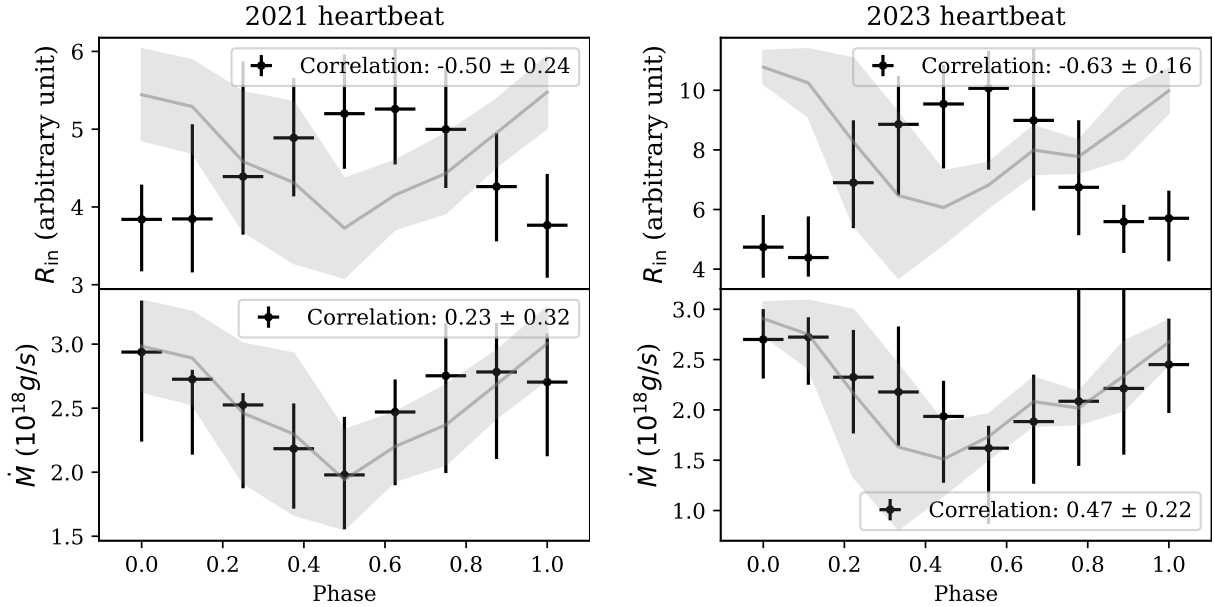


Figure 15. As in Fig. 14 but for fits with the spectral model `tbfeo` \times `thcomp` \otimes `kerdd`. Here, the inner disk radius (R_{in}) is shown in the upper panel and the mass accretion rate is shown in the lower panel. R_{in} is in arbitrary unit due to a lack of robust constraint on the distance and mass of the source (Seifina et al. 2014).

time-resolved spectral fitting of other sources reached a similar conclusion (Belloni et al. 1997; Neilsen et al. 2011; Rawat et al. 2022).

Besides the phase-resolved fitting of the heartbeat spectra, the energy dependence of the PDS properties and the lags between the photons of different energy bands can also be informative in revealing the origin of the heartbeat. We observe a significant hard lag near the heartbeat characteristic frequency of about one second (similar hard lag at \sim mHz has also been observed in other sources, e.g., GX 339–4 (Uttley et al. 2011) and MAXI J1820+070 (Uttley & Malzac 2023)). This timescale is several orders of magnitude longer than those expected for reverberation. Instead, a possible explanation for such a large lag is the viscous propagation of mass accretion fluctuations in the disk (Uttley et al. 2011; Lyubarskii 1997).

Moreover, a positive correlation between fractional rms of the heartbeat variability and energy is observed. This trend is also observed by Yang et al. (2022) to reach an energy of 100 keV. The authors conclude that these *Insight*-HXMT data constrain the origin of the heartbeat to the corona region. However, our phase-resolved fitting results do not show strong correlation between the count rate and the coronal parameters, which is also the case in the time-resolved fitting of the heartbeat state of GRS 1915+105 in Rawat et al. (2022). Instead, we suggest that disk photons have a temperature modulation, seeding variability which is magnified by the coronal Compton scattering. This could plausibly account

for the positive correlation between the fractional rms and energy. A similar scenario has also been proposed in Uttley & Malzac (2024) and supported by analytical calculations.

From the phase-resolved fitting results combined with the radiation pressure instability scenario, we can phenomenologically explain the changes of the inner disk temperature before, during, and after the heartbeat. Before the thermal viscous cycle of the heartbeat begins, the disk accretion process should be on one of the stable branches and the temperature at each radius is locally stable; at the heartbeat cycles onset, the temperature is seen to oscillate over the heartbeat pattern. Because of this, the aggregate spectrum of the heartbeat state blends a range of different thermal components (i.e., a range of disk temperatures). This results in a marked change in the temperature obtained for fitting the time-averaged observation compared to the adjacent data. This is apparent from both the 2021 and 2023 heartbeats states (see Appendix B).

6.3. The production of wind

A number of BXRBS have been found to show absorption lines in their spectra which are associated with wind features. Examples include GRS 1915+015 (Zoghbi et al. 2016; Miller et al. 2016; Liu et al. 2022), IGR J17091–3624 (Wang et al. 2024), MAXI J1803–298 (Zhang et al. 2024), as well as the subject of this paper, 4U 1630–47 (Pahari et al. 2018; Trueba et al. 2019).

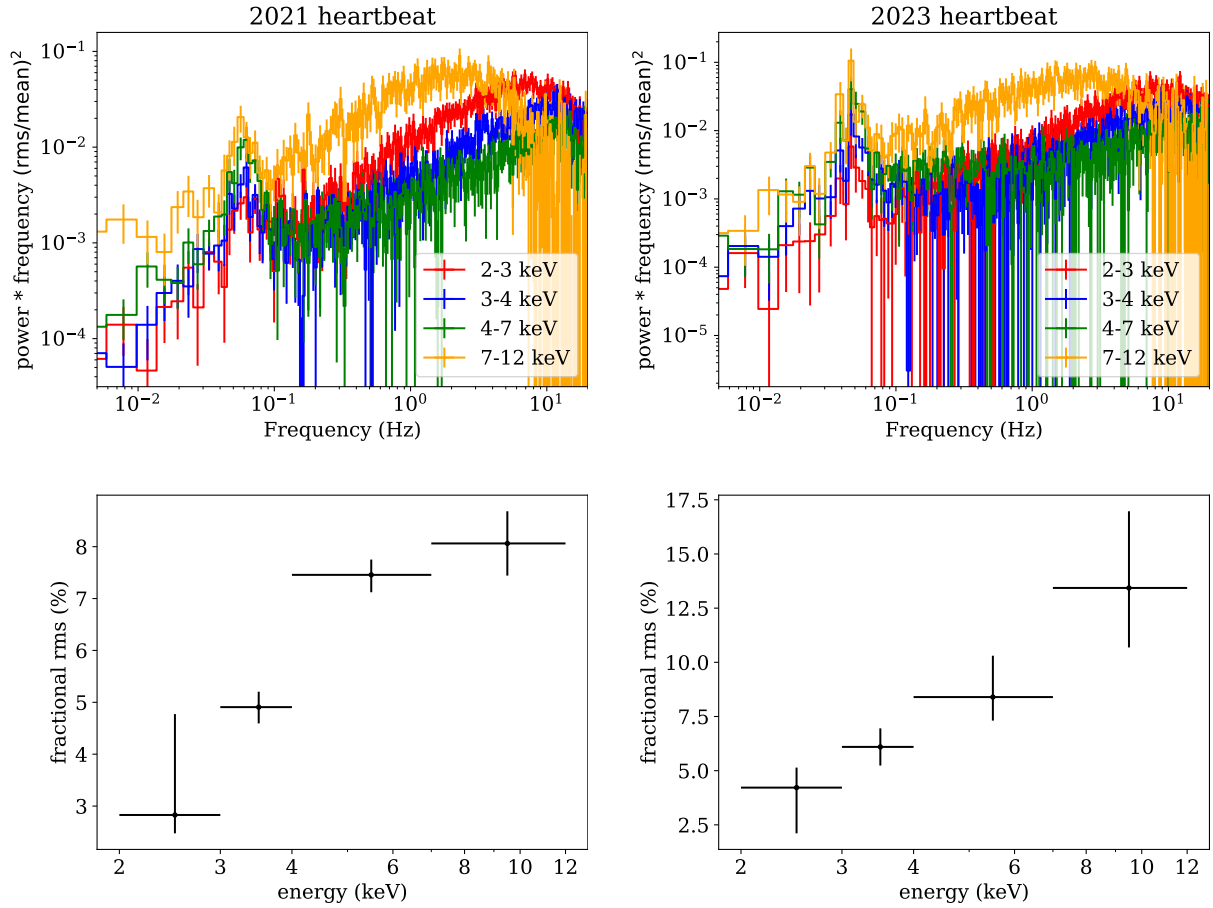


Figure 16. The energy dependence of the PDS properties of the heartbeat states in 2021 (left) and 2023 (right). Top panel: the energy-resolved PDS for 2–3 keV, 3–4 keV, 4–7 keV and 7–12 keV. Lower panel: the energy dependence of the fractional rms in the heartbeat state.

There are mainly three candidates to explain the driving mechanism for the wind: the radiation-, thermal-, or magnetic-driving (see Sect. 10 in [Done et al. 2007](#), and references therein, for a general review). In the radiation-driven model, as the luminosity approaches the Eddington-limit, the radiation pressure reduces the effective gravity (by a factor of about $1 - L/L_{\text{Edd}}$, where L_{Edd} is the Eddington luminosity of the source), thus launching the outflow. In the thermal-driven model ([Begelman et al. 1983](#)), the central illumination heats the disk to a high temperature, and the heating expands to larger radius due to the pressure gradient. At large enough radii where the thermal energy exceeds the binding energy, a wind will be produced from the outer disk. For the magnetically-driven model ([Balbus 2005a](#)), while magnetohydrodynamic (MHD) simulations shows clear presence of the wind ([Balbus 2005b](#)), a quantitative study of the relationship between the wind and magnetic field is uncertain, e.g., owing to the unknown magnetic-field topology.

Our spectral analysis shows that the wind absorption features appear in certain spectral states: the SIMS and soft state (see the HID and HRD in Fig. 2 and Fig. 3). In addition, Fig. 12 shows that the temperature of the observations with wind features is concentrated near a quite high value of about 1.5 keV, indicating the close connection between the production of wind and the strength and temperature of the thermal component. The luminosity of the source when wind features appear is well-below the peak brightness and is therefore unlikely to be super-Eddington (also found in [Trueba et al. 2019](#); [Pahari et al. 2018](#)). This indicates that the radiation pressure may not be high enough to drive the wind. In addition to the thermal-driving scenario, the magnetic-driving mechanism may also play an important role in the appearance of winds in 4U 1630–47, as is discussed in detail in [Miller et al. \(2015\)](#); [Trueba et al. \(2019\)](#).

In our study, no strong correlation between the appearance of the wind and the heartbeat is observed. For example, in the 2018 and 2022 outbursts, the wind is

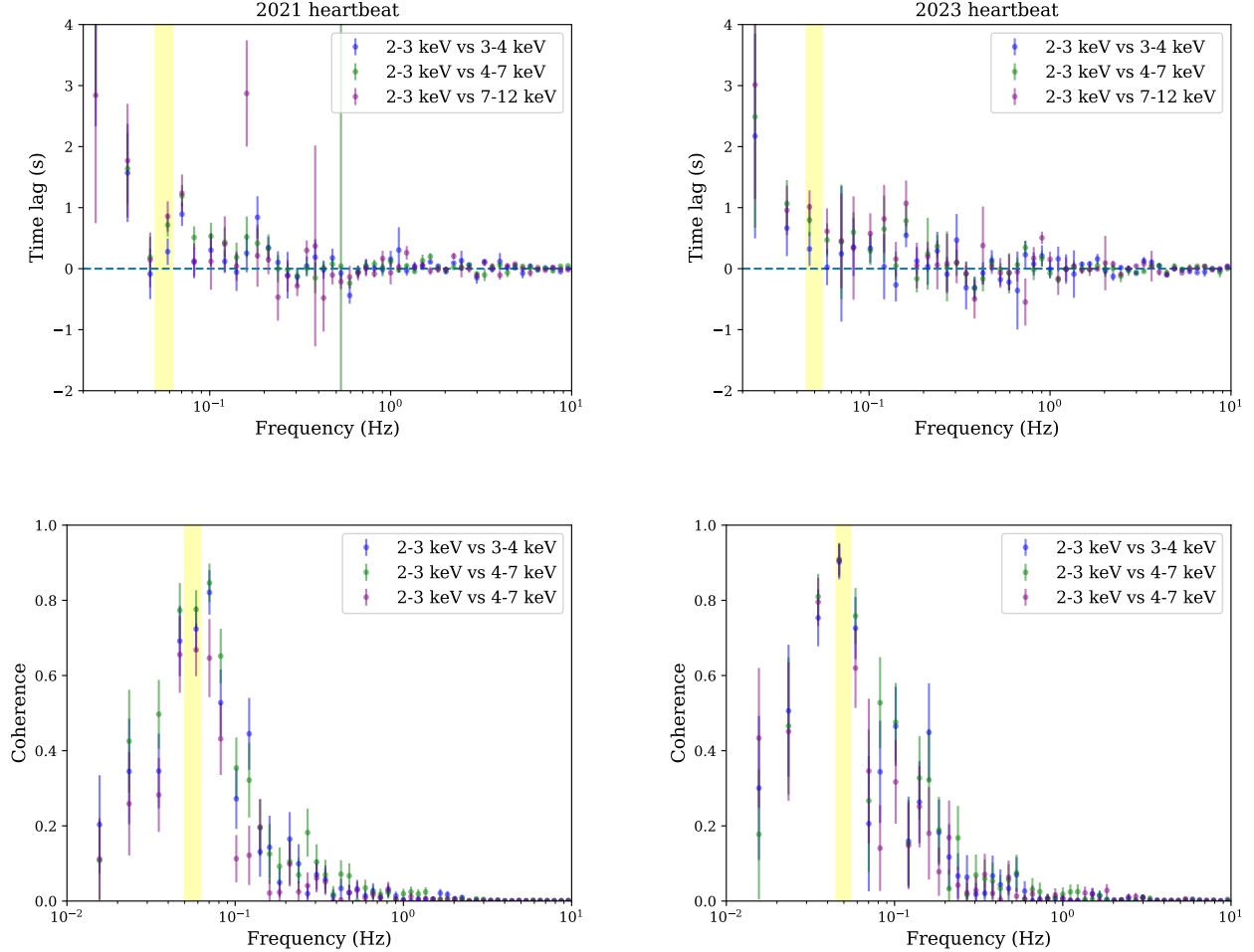


Figure 17. The energy dependence of lag (upper panels) and coherence (lower panels) of the heartbeat states in 2021 (left) and 2023 (right). The reference energy band is 2–3 keV, and the comparison bands are 3–4 keV, 4–7 keV, and 7–12 keV. The yellow region highlights the frequency range of the heartbeat oscillations (from the PDS fits). Near the characteristic frequency of the heartbeats annotated by the yellow region, a significant hard lag of ~ 1 s between 4–12 keV photons and 2–3 keV photons is clearly observed.

observed but not the heartbeat, and conversely for the 2021 outburst. In [Hori et al. \(2018\)](#); [Díaz Trigo et al. \(2014\)](#), the ionization degree of the wind of this source is observed to be positively correlated with the luminosity, and spectral wind absorption features disappear when the luminosity is extremely high and the wind is over-ionized. In our case, the heartbeat luminosity is lower than the luminosity of wind observations, therefore over-ionization may not be a plausible explanation for the absence of wind features during the heartbeats. However, in other BHXRB systems, notably [GRS 1915+015 \(Zoghbi et al. 2016\)](#) and [IGR J17091–3624 \(Wang et al. 2024\)](#), the heartbeat state is observed simultaneously with the wind, making possible a link between the instability giving rise to the heartbeat and wind production, at least for those systems.

7. CONCLUSIONS

In this paper, we present spectral and timing analysis of the *NICER* observations of the source 4U 1630–47 from 2018 to 2024. Our main results include:

1. We fit all the spectra with the disk-corona model $\text{tbfeo} \times \text{thcomp} \otimes \text{diskbb}$ and find some spectra showing broadened iron line reflection features in the HIMS and SIMS, and some showing disk wind absorption features in the SIMS and soft state. We fit the reflection spectra with `relxillCp` and find a stable and untruncated disk in the intermediate states; For the disk wind absorption features, we fit them with `zxcipcf` and find a stable, highly ionized wind with high column density across different outbursts.

2. Through the analysis of the light curves and power density spectra, we find two observations in 2021 and 2023 with heartbeat features. The light curves of these observations oscillate quasi-periodically at a frequency around 0.05 Hz and have a heartbeat-like profile. Through phase-resolved fitting of the spectra, we find the flux to be correlated with disk parameters: the inner disk temperature, inner disk radius and mass accretion rate, while no strong correlation with coronal parameters is found. This fast disk oscillation supports the inner disk radiation pressure instability as the driving mechanism of the heartbeats. Moreover, a significant hard lag on the time scale of a second is observed near the characteristic frequency of the heartbeat, which can be explained by the viscous propagation of mass accretion fluctuations in the disk. Combining the phase-resolved spectral analysis and lag analysis, the scenario where the disk-originated oscillation is then magnified by the corona scattering is

a possible explanation for the positive relationship between the fractional rms and energy.

3. The observations with disk wind features are found to have a high disk temperature, while their luminosities are well below the peak brightness (so unlikely to be super-Eddington). Accordingly, the wind is more likely to be thermally driven or magnetically driven instead of radiatively driven.

Acknowledgments – N.F. thanks Honghui Liu, Zuobin Zhang, Yujia Song, Josephine Wong and Niek Bollemeijer for useful discussions. The work of N.F. and C.B. was supported by the National Natural Science Foundation of China (NSFC), Grant No. 11973019, 12250610185, and 12261131497, and the Natural Science Foundation of Shanghai, Grant No. 22ZR1403400. O.K. acknowledges NICER GO funding 80NSSC23K1660.

APPENDIX

A. QUANTITATIVE DEFINITION OF WINDS

Besides judging from the shape of the fitting residuals, we identify spectra with wind absorption features quantitatively. We add two Gaussian functions to the continuum model `tbfeo` \times `thcomp` \otimes `diskbb`, with their centers fixed at the energies of the Fe XXV and Fe XXVI lines respectively. We calculate the equivalent width of the two absorption lines and show the upper bound of equivalent width (at a 90% confidence level) in Fig. 18. If the upper limit of the equivalent width for either of the absorption lines in a spectrum falls below zero, we identify it as exhibiting wind absorption. This quantitative criterion is consistent with our qualitative assessment.

B. HEARTBEAT SPECTRA

In Fig. 19, we present the spectra of the heartbeat state, along with spectra from observations taken before and after this state. The heartbeat spectra differ significantly from those of the nearby observations, with notable changes in the inner disk temperature (T_{in}). In 2021, T_{in} shifts from ~ 0.75 keV before the heartbeat, to ~ 1.35 keV during the heartbeat, and then to ~ 1.75 keV afterward. In 2023, T_{in} changes from ~ 1.2 keV before the heartbeat, to ~ 0.8 keV during it, and then to ~ 1.6 keV afterward.

REFERENCES

- Alabarta, K., Altamirano, D., Méndez, M., et al. 2020, *MNRAS*, 497, 3896, doi: [10.1093/mnras/staa2168](https://doi.org/10.1093/mnras/staa2168)
- Arnaud, K. A. 1996, in *Astronomical Society of the Pacific Conference Series*, Vol. 101, *Astronomical Data Analysis Software and Systems V*, ed. G. H. Jacoby & J. Barnes, 17
- Bachetti, M., & Huppenkothen, D. 2022, arXiv e-prints, arXiv:2209.07954, doi: [10.48550/arXiv.2209.07954](https://doi.org/10.48550/arXiv.2209.07954)
- Balbus, S. A. 2005a, in *Astronomical Society of the Pacific Conference Series*, Vol. 330, *The Astrophysics of Cataclysmic Variables and Related Objects*, ed. J. M. Hameury & J. P. Lasota, 185, doi: [10.48550/arXiv.astro-ph/0411281](https://doi.org/10.48550/arXiv.astro-ph/0411281)
- Balbus, S. A. 2005b, in *Astronomical Society of the Pacific Conference Series*, Vol. 330, *The Astrophysics of Cataclysmic Variables and Related Objects*, ed. J. M. Hameury & J. P. Lasota, 185, doi: [10.48550/arXiv.astro-ph/0411281](https://doi.org/10.48550/arXiv.astro-ph/0411281)

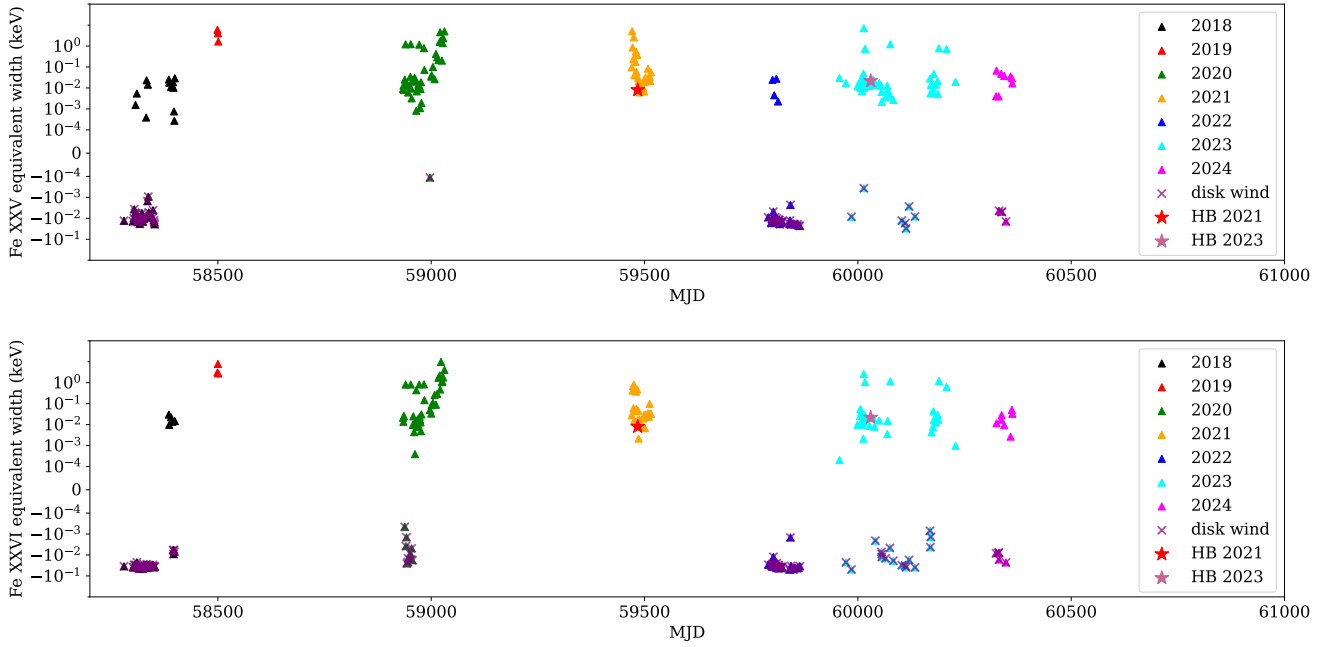


Figure 18. The upper bound of the equivalent width of the the Fe XXV (upper panel) and Fe XXVI (lower panel) absorption line. The purple crosses show the spectra we identify with wind features from a below zero upper bound of either of the two lines.

- Begelman, M. C., McKee, C. F., & Shields, G. A. 1983, *ApJ*, 271, 70, doi: [10.1086/161178](https://doi.org/10.1086/161178)
- Belloni, T., Méndez, M., King, A. R., van der Klis, M., & van Paradijs, J. 1997, *ApJL*, 488, L109, doi: [10.1086/310944](https://doi.org/10.1086/310944)
- Belloni, T. M. 2010, in *Lecture Notes in Physics*, Berlin Springer Verlag, ed. T. Belloni, Vol. 794, 53, doi: [10.1007/978-3-540-76937-8_3](https://doi.org/10.1007/978-3-540-76937-8_3)
- Belloni, T. M., & Motta, S. E. 2016, in *Astrophysics and Space Science Library*, Vol. 440, *Astrophysics of Black Holes: From Fundamental Aspects to Latest Developments*, ed. C. Bambi, 61, doi: [10.1007/978-3-662-52859-4_2](https://doi.org/10.1007/978-3-662-52859-4_2)
- Belloni, T. M., Motta, S. E., & Muñoz-Darias, T. 2011, *Bulletin of the Astronomical Society of India*, 39, 409, doi: [10.48550/arXiv.1109.3388](https://doi.org/10.48550/arXiv.1109.3388)
- Bollemeijer, N., Uttley, P., Basak, A., et al. 2024, *MNRAS*, 528, 558, doi: [10.1093/mnras/stad3912](https://doi.org/10.1093/mnras/stad3912)
- Buisson, D. J. K., Fabian, A. C., Barret, D., et al. 2019, *MNRAS*, 490, 1350, doi: [10.1093/mnras/stz2681](https://doi.org/10.1093/mnras/stz2681)
- Capitanio, F., Campana, R., De Cesare, G., & Ferrigno, C. 2015, *MNRAS*, 450, 3840, doi: [10.1093/mnras/stv687](https://doi.org/10.1093/mnras/stv687)
- Casella, P., Belloni, T., & Stella, L. 2005, *ApJ*, 629, 403, doi: [10.1086/431174](https://doi.org/10.1086/431174)
- Choudhury, M., Bhatt, N., & Bhattacharyya, S. 2015, *MNRAS*, 447, 3960, doi: [10.1093/mnras/stu2742](https://doi.org/10.1093/mnras/stu2742)
- Davis, S. W., Done, C., & Blaes, O. M. 2006, *ApJ*, 647, 525, doi: [10.1086/505386](https://doi.org/10.1086/505386)
- De Marco, B., Zdziarski, A. A., Ponti, G., et al. 2021, *A&A*, 654, A14, doi: [10.1051/0004-6361/202140567](https://doi.org/10.1051/0004-6361/202140567)
- Díaz Trigo, M., Migliari, S., Miller-Jones, J. C. A., & Guainazzi, M. 2014, *A&A*, 571, A76, doi: [10.1051/0004-6361/201424554](https://doi.org/10.1051/0004-6361/201424554)
- Done, C., Gierliński, M., & Kubota, A. 2007, *A&A Rv*, 15, 1, doi: [10.1007/s00159-007-0006-1](https://doi.org/10.1007/s00159-007-0006-1)
- Ebisawa, K., Życki, P., Kubota, A., Mizuno, T., & Watarai, K.-y. 2003, *ApJ*, 597, 780, doi: [10.1086/378586](https://doi.org/10.1086/378586)
- Fabian, A. C., Parker, M. L., Wilkins, D. R., et al. 2014, *MNRAS*, 439, 2307, doi: [10.1093/mnras/stu045](https://doi.org/10.1093/mnras/stu045)
- Fan, N., Li, S., Zhan, R., et al. 2024, *ApJ*, 969, 61, doi: [10.3847/1538-4357/ad49a1](https://doi.org/10.3847/1538-4357/ad49a1)
- Ferland, G. J., Chatzikos, M., Guzmán, F., et al. 2017, *RMxAA*, 53, 385, doi: [10.48550/arXiv.1705.10877](https://doi.org/10.48550/arXiv.1705.10877)
- García, J., Dauser, T., Lohfink, A., et al. 2014, *ApJ*, 782, 76, doi: [10.1088/0004-637X/782/2/76](https://doi.org/10.1088/0004-637X/782/2/76)
- Gatuzz, E., Díaz Trigo, M., Miller-Jones, J. C. A., & Migliari, S. 2019, *MNRAS*, 482, 2597, doi: [10.1093/mnras/sty2850](https://doi.org/10.1093/mnras/sty2850)
- Heil, L. M., Uttley, P., & Klein-Wolt, M. 2015, *MNRAS*, 448, 3339, doi: [10.1093/mnras/stv191](https://doi.org/10.1093/mnras/stv191)
- Homan, J., & Belloni, T. 2005, *Ap&SS*, 300, 107, doi: [10.1007/s10509-005-1197-4](https://doi.org/10.1007/s10509-005-1197-4)

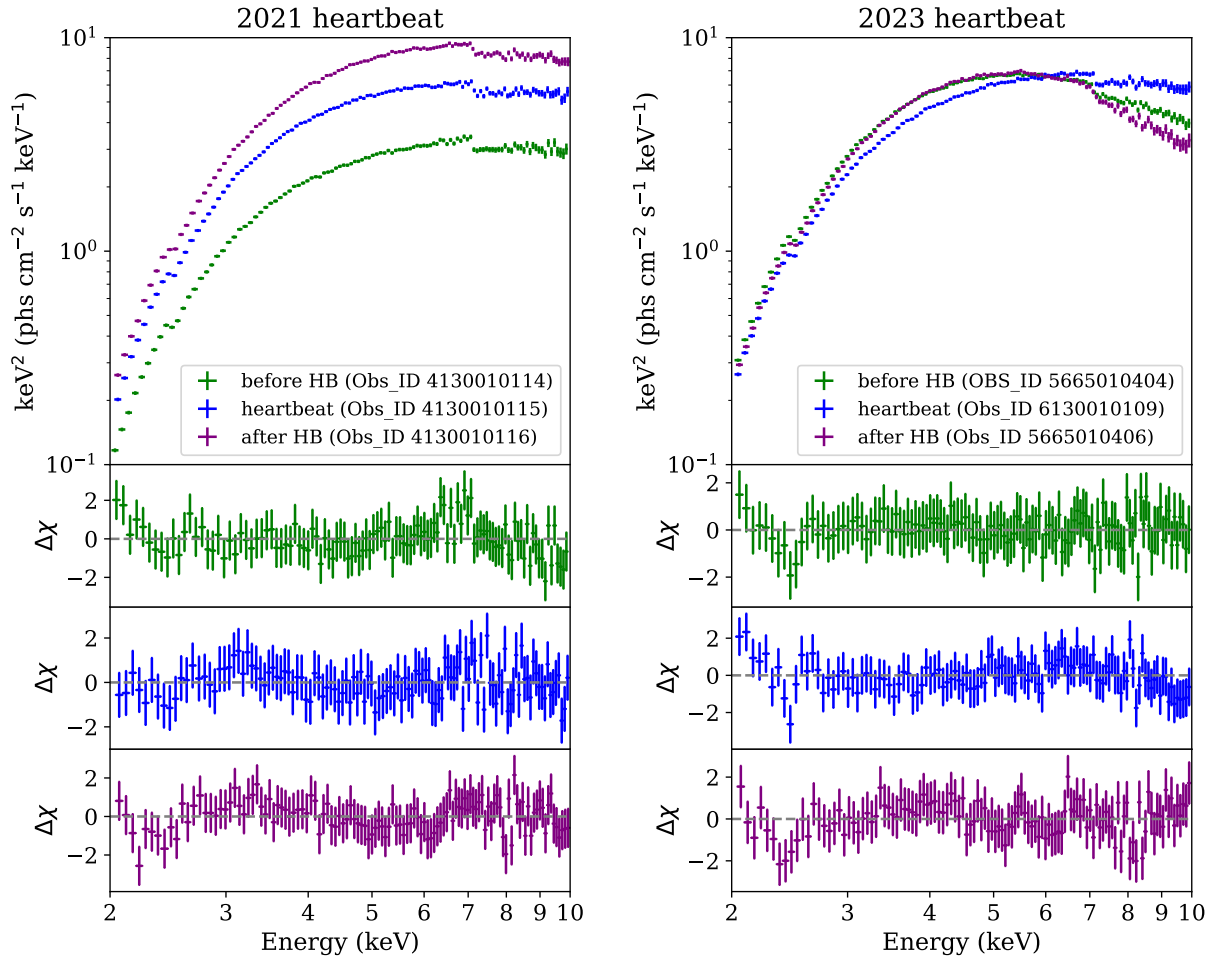


Figure 19. The upper panel shows the spectra of the heartbeat state in 2021 (left panel) and 2023 (right panel), along with spectra from observations taken before and after the heartbeat state. The lower panels show the residuals of the fits of these spectra with the continuum model $\text{tbfeo} \times \text{thcomp} \otimes \text{diskbb}$.

Hori, T., Ueda, Y., Done, C., Shidatsu, M., & Kubota, A. 2018, *The Astrophysical Journal*, 869, 183, doi: [10.3847/1538-4357/aaea5e](https://doi.org/10.3847/1538-4357/aaea5e)

Ingram, A. R., & Motta, S. E. 2019, *NewAR*, 85, 101524, doi: [10.1016/j.newar.2020.101524](https://doi.org/10.1016/j.newar.2020.101524)

Jones, C., Forman, W., Tananbaum, H., & Turner, M. J. L. 1976, *ApJL*, 210, L9, doi: [10.1086/182291](https://doi.org/10.1086/182291)

Katoch, T., Baby, B. E., Nandi, A., et al. 2021, *MNRAS*, 501, 6123, doi: [10.1093/mnras/staa3756](https://doi.org/10.1093/mnras/staa3756)

King, A. L., Walton, D. J., Miller, J. M., et al. 2014, *ApJL*, 784, L2, doi: [10.1088/2041-8205/784/1/L2](https://doi.org/10.1088/2041-8205/784/1/L2)

Kubota, A., & Makishima, K. 2004, *ApJ*, 601, 428, doi: [10.1086/380433](https://doi.org/10.1086/380433)

Kubota, A., Tanaka, Y., Makishima, K., et al. 1998, *PASJ*, 50, 667, doi: [10.1093/pasj/50.6.667](https://doi.org/10.1093/pasj/50.6.667)

Kushwaha, A., Jayasurya, K. M., Agrawal, V. K., & Nandi, A. 2023, *MNRAS*, 524, L15, doi: [10.1093/mnras/sladd070](https://doi.org/10.1093/mnras/sladd070)

Li, L.-X., Zimmerman, E. R., Narayan, R., & McClintock, J. E. 2005, *ApJS*, 157, 335, doi: [10.1086/428089](https://doi.org/10.1086/428089)

Lightman, A. P., & Eardley, D. M. 1974, *ApJL*, 187, L1, doi: [10.1086/181377](https://doi.org/10.1086/181377)

Liu, H., Fu, Y., Bambi, C., et al. 2022, *Astrophys. J.*, 933, 122, doi: [10.3847/1538-4357/ac74b1](https://doi.org/10.3847/1538-4357/ac74b1)

Liu, H., Bambi, C., Jiang, J., et al. 2023, *ApJ*, 950, 5, doi: [10.3847/1538-4357/acca17](https://doi.org/10.3847/1538-4357/acca17)

Lyubarskii, Y. E. 1997, *MNRAS*, 292, 679, doi: [10.1093/mnras/292.3.679](https://doi.org/10.1093/mnras/292.3.679)

Ma, X., Tao, L., Zhang, S.-N., et al. 2021, *Nature Astronomy*, 5, 94, doi: [10.1038/s41550-020-1192-2](https://doi.org/10.1038/s41550-020-1192-2)

Miller, J. M., Fabian, A. C., Kaastra, J., et al. 2015, *ApJ*, 814, 87, doi: [10.1088/0004-637X/814/2/87](https://doi.org/10.1088/0004-637X/814/2/87)

Miller, J. M., Raymond, J., Fabian, A. C., et al. 2016, *ApJL*, 821, L9, doi: [10.3847/2041-8205/821/1/L9](https://doi.org/10.3847/2041-8205/821/1/L9)

Mitsuda, K., Inoue, H., Koyama, K., et al. 1984, *PASJ*, 36, 741

- Neilsen, J., Remillard, R. A., & Lee, J. C. 2011, *ApJ*, 737, 69, doi: [10.1088/0004-637X/737/2/69](https://doi.org/10.1088/0004-637X/737/2/69)
- . 2012, *ApJ*, 750, 71, doi: [10.1088/0004-637X/750/1/71](https://doi.org/10.1088/0004-637X/750/1/71)
- Pahari, M., Bhattacharyya, S., Rao, A. R., et al. 2018, *ApJ*, 867, 86, doi: [10.3847/1538-4357/aae53b](https://doi.org/10.3847/1538-4357/aae53b)
- Plant, D. S., Fender, R. P., Ponti, G., Muñoz-Darias, T., & Coriat, M. 2014, *MNRAS*, 442, 1767, doi: [10.1093/mnras/stu867](https://doi.org/10.1093/mnras/stu867)
- Raj, A., & Nixon, C. J. 2021, *ApJ*, 909, 82, doi: [10.3847/1538-4357/abdc25](https://doi.org/10.3847/1538-4357/abdc25)
- Ratheesh, A., Dovčiak, M., Krawczynski, H., et al. 2024, *ApJ*, 964, 77, doi: [10.3847/1538-4357/ad226e](https://doi.org/10.3847/1538-4357/ad226e)
- Rawat, D., Misra, R., Jain, P., & Yadav, J. S. 2022, *MNRAS*, 511, 1841, doi: [10.1093/mnras/stac154](https://doi.org/10.1093/mnras/stac154)
- Reeves, J., Done, C., Pounds, K., et al. 2008, *MNRAS*, 385, L108, doi: [10.1111/j.1745-3933.2008.00443.x](https://doi.org/10.1111/j.1745-3933.2008.00443.x)
- Remillard, R. A., Morgan, E. H., McClintock, J. E., Bailyn, C. D., & Orosz, J. A. 1999, *ApJ*, 522, 397, doi: [10.1086/307606](https://doi.org/10.1086/307606)
- Remillard, R. A., Loewenstein, M., Steiner, J. F., et al. 2022, *AJ*, 163, 130, doi: [10.3847/1538-3881/ac4ae6](https://doi.org/10.3847/1538-3881/ac4ae6)
- Seifina, E., Titarchuk, L., & Shaposhnikov, N. 2014, *ApJ*, 789, 57, doi: [10.1088/0004-637X/789/1/57](https://doi.org/10.1088/0004-637X/789/1/57)
- Shimura, T., & Takahara, F. 1995, *ApJ*, 445, 780, doi: [10.1086/175740](https://doi.org/10.1086/175740)
- Sriram, K., Rao, A. R., & Choi, C. S. 2016, *ApJ*, 823, 67, doi: [10.3847/0004-637X/823/1/67](https://doi.org/10.3847/0004-637X/823/1/67)
- Steiner, J. F., McClintock, J. E., Remillard, R. A., et al. 2010, *ApJL*, 718, L117, doi: [10.1088/2041-8205/718/2/L117](https://doi.org/10.1088/2041-8205/718/2/L117)
- Stiele, H., & Kong, A. K. H. 2020, *ApJ*, 889, 142, doi: [10.3847/1538-4357/ab64ef](https://doi.org/10.3847/1538-4357/ab64ef)
- Trudolyubov, S. P., Borozdin, K. N., & Friedhorsky, W. C. 2001, *MNRAS*, 322, 309, doi: [10.1046/j.1365-8711.2001.04073.x](https://doi.org/10.1046/j.1365-8711.2001.04073.x)
- Trueba, N., Miller, J. M., Kaastra, J., et al. 2019, *ApJ*, 886, 104, doi: [10.3847/1538-4357/ab4f70](https://doi.org/10.3847/1538-4357/ab4f70)
- Uttley, P., & Malzac, J. 2023, arXiv e-prints, arXiv:2312.08302, doi: [10.48550/arXiv.2312.08302](https://doi.org/10.48550/arXiv.2312.08302)
- . 2024, *MNRAS*, doi: [10.1093/mnras/stae2514](https://doi.org/10.1093/mnras/stae2514)
- Uttley, P., Wilkinson, T., Cassatella, P., et al. 2011, *MNRAS*, 414, L60, doi: [10.1111/j.1745-3933.2011.01056.x](https://doi.org/10.1111/j.1745-3933.2011.01056.x)
- van der Klis, M. 1995, in *X-ray Binaries*, ed. W. H. G. Lewin, J. van Paradijs, & E. P. J. van den Heuvel, 252–307
- Verner, D. A., Ferland, G. J., Korista, K. T., & Yakovlev, D. G. 1996, *ApJ*, 465, 487, doi: [10.1086/177435](https://doi.org/10.1086/177435)
- Wang, J., Mastroserio, G., Kara, E., et al. 2021, *ApJL*, 910, L3, doi: [10.3847/2041-8213/abec79](https://doi.org/10.3847/2041-8213/abec79)
- Wang, J., Kara, E., García, J. A., et al. 2024, *ApJ*, 963, 14, doi: [10.3847/1538-4357/ad1595](https://doi.org/10.3847/1538-4357/ad1595)
- Wang-Ji, J., García, J. A., Steiner, J. F., et al. 2018, *ApJ*, 855, 61, doi: [10.3847/1538-4357/aaa974](https://doi.org/10.3847/1538-4357/aaa974)
- Wilms, J., Allen, A., & McCray, R. 2000, *The Astrophysical Journal*, 542, 914, doi: [10.1086/317016](https://doi.org/10.1086/317016)
- Yang, Z.-x., Zhang, L., Huang, Y., et al. 2022, *ApJ*, 937, 33, doi: [10.3847/1538-4357/ac84d6](https://doi.org/10.3847/1538-4357/ac84d6)
- Zdziarski, A. A., Szanecki, M., Poutanen, J., Gierliński, M., & Biernacki, P. 2020, *MNRAS*, 492, 5234, doi: [10.1093/mnras/staa159](https://doi.org/10.1093/mnras/staa159)
- Zhang, Z., Bambi, C., Liu, H., et al. 2024. <https://arxiv.org/abs/2402.10315>
- Zoghbi, A., Miller, J. M., King, A. L., et al. 2016, *ApJ*, 833, 165, doi: [10.3847/1538-4357/833/2/165](https://doi.org/10.3847/1538-4357/833/2/165)
- Życki, P. T., Done, C., & Smith, D. A. 1999, *MNRAS*, 309, 561, doi: [10.1046/j.1365-8711.1999.02885.x](https://doi.org/10.1046/j.1365-8711.1999.02885.x)